

High-resolution spectroscopy of the blue compact dwarf galaxy Haro 15 – I. Internal kinematics

Verónica Firpo,^{1★} Guillermo Bosch,^{1†} Guillermo F. Hägele,^{1,2‡} Ángeles I. Díaz²
and Nidia Morrell³

¹Facultad de Ciencias Astronómicas y Geofísicas, Universidad Nacional de la Plata, Paseo del Bosque s/n, 1900 La Plata, Argentina

²Departamento de Física Teórica, C-XI, Universidad Autónoma de Madrid, 28049 Madrid, Spain

³Las Campanas Observatory, Carnegie Observatories, Casilla 601, La Serena, Chile

Accepted 2011 March 1. Received 2011 March 1; in original form 2010 December 14

ABSTRACT

Using echelle spectroscopy, obtained at Las Campanas Observatory, we present a detailed study of the internal kinematics of the nebular material in multiple knots of the blue compact dwarf galaxy Haro 15. A detailed analysis of the complex emission-line profiles shows the presence of an underlying broad component in almost all knots, and the brightest star-forming region shows unmistakable signs for the presence of two distinct narrow kinematical components. We also study the information that our analysis provides regarding the motion of the individual knots in the Haro 15 galaxy potential, confirming that they follow galactic rotation. Finally, we examine the relation between their velocity dispersion and luminosity, finding that almost all knots follow the relation for virialized systems. This holds for the strong narrow components identified in complex fits and for single profile fits, although the latter show a flatter slope. In agreement with previous findings, in this paper we show that the existence of multiple kinematical components among massive starbursts cannot be overlooked, as it has a noticeable effect on any subsequent analysis that relies on basic parameters.

Key words: H II regions – galaxies: individual: Haro 15 – galaxies: starburst.

1 INTRODUCTION

Already in the original list of blue galaxies with emission lines by Haro (1956) who described this object as a ‘minute cometary nebula’, Haro 15 was later included in several compilations of blue compact galaxies (BCGs). Several studies at all frequencies have been carried out of this object. In particular, optical spectroscopy was analysed by Hunter & Gallagher (1985), Mazzarella, Bothun & Boroson (1991), Kong et al. (2002) and Shi et al. (2005), among others. Owing to the detection of the He II $\lambda 4686$ emission line by Kovo & Contini (1999), Schaerer, Contini & Pindao (1999) have classified this galaxy as a Wolf–Rayet (WR) galaxy. López-Sánchez & Esteban (2010) also found a blue WR bump supporting the WR nature of Haro 15. The H α image shown in Cairós et al. (2001a) shows a knotty morphology with the starburst region resolved into a large number of clumps which appear scattered over the entire galaxy. The integrated H α luminosity yields a star formation rate (SFR) of $3.3 \text{ M}_{\odot} \text{ yr}^{-1}$ (López-Sánchez & Esteban 2008). López-Sánchez (2010) analysed the SFR in Haro 15 using multi-wavelength data. The derived values using H α , far-infrared (FIR)

and radio data are very similar, but the value derived using the far-ultraviolet (FUV) luminosity is twice the others, confirming that a young stellar population is dominating the light of the galaxy and suggesting that the starburst phenomenon in Haro 15 started some time ago (at least 100 Myr ago). From the morphological point of view, Haro 15 has been classified as an (R)SB0 peculiar galaxy by de Vaucouleurs et al. (1991) and in fact, in the deep images taken with the 2.2-m CAHA telescope shown by López-Sánchez & Esteban (2008), the spiral morphology of the galaxy can easily be appreciated. Two high surface brightness concentrations can be distinguished, named A and C by the authors. Both show blue colours and high FUV emission, indicative of recent and ongoing star formation activity, further supported by the presence of the WR features.

Long slit optical spectroscopy of Haro 15 has been presented in López-Sánchez & Esteban (2009) covering four main regions in the galaxy: the centre (named C by the authors) and three bright regions located ESE (named A), WNW (named D) and NE (named B). The spectrum of the central region shows strong nebular emission lines and prominent stellar absorption wings in the H I Balmer lines, evidence of an underlying stellar population which the authors estimate to be around 500 Myr old. Only emission lines are seen in regions A and B and the spectrum of region D is too noisy to be analysed. These authors derived an oxygen abundance of $12 + \log(\text{O}/\text{H}) = 8.37 \pm 0.10$ and 8.10 ± 0.06 for regions A and B, respectively.

*E-mail: vfirpo@fcaglp.unlp.edu.ar

†IALP-CONICET, Argentina.

‡CONICET, Argentina.

Based on these data the authors conclude that all the observed knots can be classified as typical H II regions.

Haro 15 has an absolute magnitude $M_B = -20.69$, a surface brightness $\mu_B = 18.56 \text{ mag arcsec}^{-2}$ and a colour $B - V = 0.33$ (Cairós et al. 2001a). At a distance of 86.6 Mpc (de Vaucouleurs et al. 1991), Haro 15 meets the criteria for a luminous compact blue galaxy (LCBG; Hoyos et al. 2004) despite the fact that its brightness distribution shows an exponential profile with a scalelength of 1.37 kpc. The nature of this type of galaxy is not yet clear since they probably constitute a mixed population of starburst galaxies. Some authors suggest that LCBGs might represent the final outcome of a merger between a dwarf elliptical and a gas-rich dwarf galaxy or H I cloud (Östlin 1998; Cumming et al. 2008). The interactions taking place during the merging process would act as the starburst trigger (see e.g. López-Sánchez, Esteban & Rodríguez 2004; López-Sánchez, Esteban & García-Rojas 2006). The images of Haro 15 showing two separated nuclei surrounded by a more regular, roughly elliptical envelope with twisted isophotes, together with different features and faint extensions as reported by Cairós et al. (2001a), give support to this picture. Other galaxy properties like different kinematics and chemical abundances between regions A and B may also indicate that Haro 15 is probably experiencing a minor merger (López-Sánchez 2010). On the other hand, a reliable determination of the mass of this kind of object is needed in order to decide on the evolutionary path they may follow: becoming dwarf spheroidal galaxies (Hoyos et al. 2007) or the bulges of small spirals (Hammer et al. 2001). However, interactions and mergers, as well as feedback processes resulting from intense star formation, might be reflected in a peculiar gas kinematics that prevent the derivation of their dynamical masses from the gas velocity widths.

Echelle spectroscopy provides a means to look for kinematically different components in the emission lines of the ionized gas since it reaches the spectral resolution needed to resolve the presence of structures within the emission-line profile, usually masked by its large supersonic width.

In Firpo et al. (2010) we observed a residual presence in the wings of several lines when fitting single Gaussian profiles to the emission lines observed in the giant H II regions within the galaxies NGC 7479 and 6070. Based on the several studies that have been proposed in the literature to interpret the existence of the broad supersonic component measured in the emission-line profile of giant H II regions, and whenever possible, we have evaluated the possible presence of a broad component (Muñoz-Tuñón et al. 1996; Melnick, Tenorio-Tagle & Terlevich 1999; Hägele et al. 2007; Hägele et al. 2009, 2010, among others) or two symmetric low-intensity components in the fit to the observed emission-line profile widths (Chu & Kennicutt 1994; Relaño & Beckman 2005; Rozas et al. 2006). In the present work, we have also found that all Haro 15 regions show evidence of wing broadening evident mainly in the H α line and confirmed in other emission lines. Another common feature of giant H II regions is the supersonic width of their emission-line profiles, although the origin of these velocities is not yet clear (Terlevich & Melnick 1981; Hippelein 1986; Roy, Arsenault & Joncas 1986). A relation between H α luminosity and velocity dispersion of the form $L(\text{H}\alpha) \propto \sigma^4$ is expected under the assumption of a gravitational origin of the ionized gas dynamics. Therefore, a study of the implications that the existence of several kinematically distinct components has on the $L(\text{H}\alpha)$ versus σ relation is of great value.

In this paper we present echelle spectroscopy obtained with the 100-inch du Pont telescope at Las Campanas Observatory (LCO) of five different positions across Haro 15 which provide a velocity

resolution of about 12 km s^{-1} allowing the identification of different kinematical components of the gas and the measurement of their corresponding velocity dispersions. This study is part of a project to obtain high spectral resolution echelle data to determine the nature of giant H II regions visible from the southern hemisphere and analyse the physical conditions of the ionized gas of these regions and blue compact dwarf galaxies. In Section 2 we present the observations and the data reduction. Section 3 presents the analysis of the emission-line profiles and discusses the results. Finally, the summary and conclusions of this work are given in Section 4.

2 OBSERVATIONS AND DATA REDUCTION

High-resolution spectroscopy of Haro 15 was obtained using an echelle spectrograph attached to the 100-inch du Pont telescope, LCO, on 2006 July 19 and 20. The spectral range covered by the observations was from 3400 to 10 000 Å. Observing conditions were good, with an average of 1 arcsec seeing and photometric nights. A 2×2 binning was applied to the CCD in order to minimize the read-out contribution to the final spectrum noise. With 1 arcsec effective slit width and 4 arcsec slit length, the spectral resolution achieved in our du Pont echelle data was $R \simeq 25\,000$: $\Delta\lambda = 0.25 \text{ Å}$ at $\lambda 6000 \text{ Å}$, as measured from the full width at half-maximum (FWHM) of the Th–Ar comparison lines taken for wavelength calibration purposes. This translates into a velocity resolution of $\sim 12 \text{ km s}^{-1}$. Considering the distance to Haro 15 and that the spatial resolution is limited by seeing, the smallest structure that can be resolved is 0.43 kpc ($\sim 1 \text{ arcsec} \sim 1.93 \text{ pixel}$).

Five different regions in Haro 15 were observed as shown in Fig. 1. The spectra were obtained as single exposures of 1800 s.

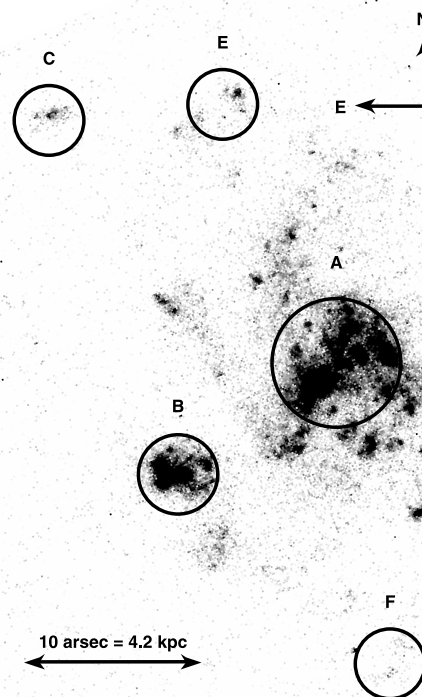


Figure 1. Finding chart for the giant H II region candidates observed in Haro 15, identified by circles and labelled following Cairós et al. (2001b). The Wide Field Planetary Camera 2 H α image was obtained from the Multimission Archive at the Space Telescope Science Institute (MAST).

Table 1. Journal of observations. The identifications in the first column correspond to the nomenclature used in this paper, following and extending that in Cairós et al. (2001b); columns 2 and 3 list the observation date and the airmass, respectively; columns 4 and 5 show the distance to the galactic centre in arcsec and kpc, respectively, and finally, column 6 lists the identification of the regions given in López-Sánchez & Esteban (2008) referred to as LS notation. The exposure time for each region was 1800 s.

Knots	Date	sec z	Dist. (arcsec)	Dist. (kpc)	LS
Haro 15 A	2006 July 19	1.2	0	0	C
Haro 15 B	2006 July 19	1.1	11	4.62	A
Haro 15 C	2006 July 19	1.1	20	8.4	B
Haro 15 E	2006 July 20	1.2	16	6.72	...
Haro 15 F	2006 July 20	1.1	17	7.14	...

CALSPEC spectrophotometric standard star Feige 110 (Bohlin, Dickinson & Calzetti 2001) was also observed for flux calibration purposes with an exposure time of 1200 s. In addition, Th–Ar comparison spectra, milky flats (sky flats obtained with a diffuser, during the afternoon) and bias frames were taken every night. A journal of observations is shown in Table 1.

The data analysis was carried out using the IRAF¹ software. After bias subtraction and flat-field corrections by means of milky flats the bidimensional images were corrected for cosmic rays using the task COSMICRAYS which detects and removes cosmic rays using a flux ratio algorithm. The corrected data were reduced by IRAF routines following procedures similar to those described in Firpo, Bosch & Morrell (2005).

At the end of the process, we compared the red end of the wavelength-calibrated spectra with the night-sky spectrum by Osterbrock et al. (1996). This turned out to be a very reliable confirmation of the goodness of the wavelength solution, and we checked that differences between our wavelengths and the sky line wavelengths were below 0.04 Å.

Flux calibration was achieved by observing the CALSPEC spectrophotometric standard star Feige 110 (Bohlin et al. 2001) whose flux was tabulated every 2 Å. Despite its relatively low brightness ($V = 11.83$), Feige 110 is ideal for calibrating high-resolution echelle spectra. The amount of defined intervals within an echelle order ranged from four to 12, depending on the quality of the spectrum. The flux calibrations were performed as described in Firpo et al. (2005).

3 RESULTS AND DISCUSSION

3.1 Line profile analysis

We identified the hydrogen recombination lines, such as H α and H β , and collisionally excited lines, such as [N II] $\lambda\lambda 6548, 6584$, [S II] $\lambda\lambda 6717, 6731$, present in the spectra, making use of the known redshift, $z = 0.021371$, for Haro 15 (de Vaucouleurs et al. 1991). The strong lines were used to analyse the structure of velocity profiles as they allow us to verify the existence of more than one component as described in Firpo et al. (2010). The adopted laboratory wavelengths were taken from the work of García-Rojas et al. (2005).

From the echelle calibrated spectrum, we cut the wavelength range where a given emission line is and we transformed from wavelength to velocity plane using the Doppler correction. By measuring

the central velocity (wavelength) and width of several emission lines we determined the radial velocities and velocity dispersions of the ionized gas in the different star-forming regions of Haro 15. The radial velocity and the intrinsic velocity dispersion (σ_{int}), corrected for the instrumental and thermal contributions of each emission line, were also derived. For these observations we considered $\sigma_i = 5.2 \text{ km s}^{-1}$ as the instrumental width. The thermal contribution was derived from Boltzmann’s equation ($\sigma_t = 2kT/m_a$), where k is Boltzmann’s constant, T the kinetic temperature ($T \simeq 10^4 \text{ K}$) and m_a the atomic mass of the corresponding element. Although a detailed determination of the electron density and temperatures, and chemical ionic and total abundances for each region will be presented in Hägele et al. (in preparation), small changes of a few hundred degrees do not noticeably modify this correction, as previously discussed in Firpo et al. (2010). The fluxes were derived from the amplitude (A) and the FWHM of the Gaussian profile obtained in the component fitting ($F = 1.0645 \times A \times \text{FWHM}$), and the corresponding errors were estimated taking into account the errors in these two parameters.

As already reported by Firpo and collaborators, in the present work we have also found that all Haro 15 emission knots show evidence of wing broadening, which is always found in the H α line profiles and is usually also observed in the profiles of the bright emission lines. Making use of the iterative fitting of multiple Gaussian profiles, we evaluated the presence of a broad component and more than one narrow component present in the emission-line profile. In this case, we fitted a broad component, explaining the integral profile wings for all regions.

In the following subsections we will discuss our findings for each knot resulting from the profile fits.

3.1.1 Haro 15 A

In our high-resolution spectra Haro 15 A shows a complex structure which, although evident in radial velocity space, could not be spatially resolved.

We identified and fitted Gaussian profiles to the H β , [O III] $\lambda 5007$, [N II] $\lambda 6548$, H α , [N II] $\lambda 6584$ and [S II] $\lambda 6717$ lines in this knot with NGAUSSFIT routines. The Gaussian fits of these emission line profiles are shown in Figs 2 and 3. The Gaussian fits in the profiles reveal the presence of two distinctly separated kinematical components labelled narrow 1 and 2 (n1 and n2). Component n1 shows a profile slightly broader than component n2 ($\sigma_{\text{int}} \simeq 28$ and 24 km s^{-1} , respectively), and both components show a relatively large spread in individual radial velocities among the different emission lines present in the spectrum. The reliability of these values is confirmed when we improve the profile fitting using NGAUSSFIT which in turn yields values for the profile width of each component. It is worth noting that, although the profile fitting to the [O III] lines shows similar overall results, the n2 components show the broader profile, opposite to what is found for the other emission lines. This could be related to a different kinematic behaviour of the highly ionized gas, although this needs to be confirmed for other high excitation lines.

Always considering the presence of two distinct components with different radial velocities, the overall fit continues to show the presence of a residual in the emission-line wings. Following the procedures outlined in Firpo et al. (2010), we are able to fit a broad component, with a velocity dispersion of about 78 km s^{-1} from the H α emission line and slightly lower from the rest of the lines. Table 2 shows the parameters for the three components that fit the global profile. Individual Gaussian component fluxes are listed

¹ Image Reduction and Analysis Facility (IRAF), distributed by NOAO, operated by AURA, Inc., under agreement with the NSF.

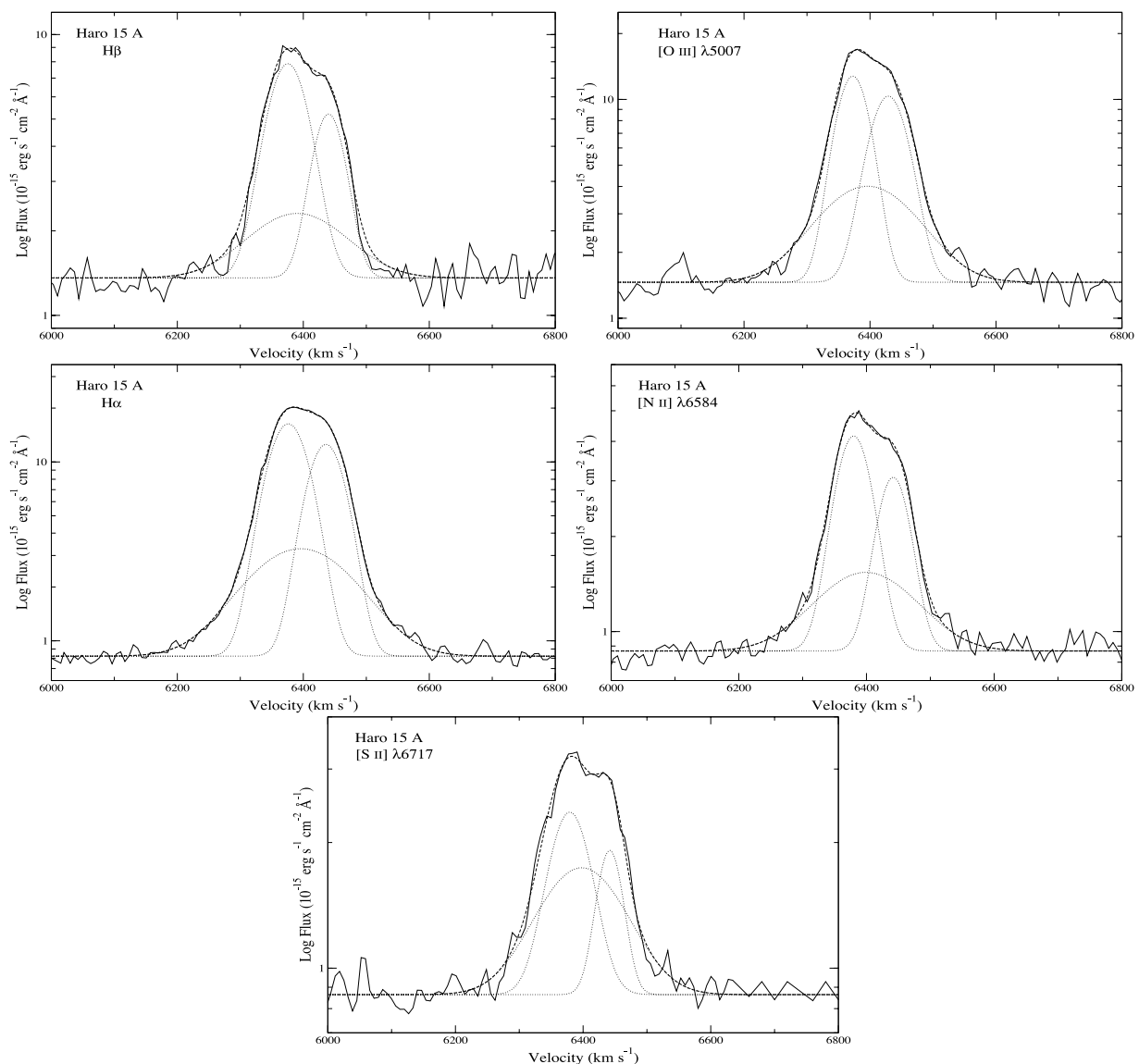


Figure 2. Strongest emission lines from the Haro 15 A spectrum. Each panel includes a flux-calibrated spectrum, where the individual x -axis has been normalized to the observed radial velocity for comparison purposes. To enhance details at low-luminosity levels, the y -axes are shown in logarithmic scale. From top to bottom and left to right: H β , [O III] λ 5007, H α , [N II] λ 6584 and [S II] λ 6717.

as fractional emission measures (EM_f) relative to the total line flux following the work by Relaño & Beckman (2005). The sum of these individual fluxes, which we will hereafter refer to as overall H α flux, uncorrected for reddening, is found to be $(5.49 \pm 0.05) \times 10^{-14} \text{ erg s}^{-1} \text{ cm}^{-2}$.

In Fig. 2 we show the `NGAUSSFIT` fitting done with three different Gaussian components in the emission lines which have enough signal to provide a reliable fit. The validity of the profile multiplicity and broadening is checked over the different emission lines, becoming more evident for the strongest emission lines. Fig. 3 shows the excellent agreement among individual fits for the most intense emission lines in knot A.

The top panel in Fig. 4 shows the spatial profile of the H α emission line in knot A. Two distinct zones are clearly distinguished, separated by $1.72 \text{ arcsec} \sim 0.72 \text{ kpc}$. We have performed additional extractions of these two zones (labelled A I and A II) individually. Inspection of the individual plots displayed in the bottom panels show that the kinematical structure is dominated by region A I,

somewhat expected as it is brighter than region A II, which exhibits a more simple emission profile in turn. High spatial resolution integrated field spectroscopy is needed to disentangle this complex behaviour.

3.1.2 Haro 15 B

The spectrum of region B is dominated by nebular emission lines, where we detected and measured [O III] λ 4363 and He II λ 4686. We identified and fitted Gaussian profiles to the H β , [O III] $\lambda\lambda$ 4959, 5007, [N II] λ 6548, H α , [N II] λ 6584 and [S II] $\lambda\lambda$ 6717, 6731 lines in this region using `NGAUSSFIT`. It is interesting to note that, although from inspection of the Wide Field Planetary Camera 2 image shown in Fig. 1 a complex structure of region B is apparent, this is not reflected in the kinematical behaviour of the region, since it is possible to fit a single Gaussian component with a velocity dispersion of 20 km s^{-1} . Nevertheless, the profile fittings show the presence of a residual in the emission-line wings that we were able to

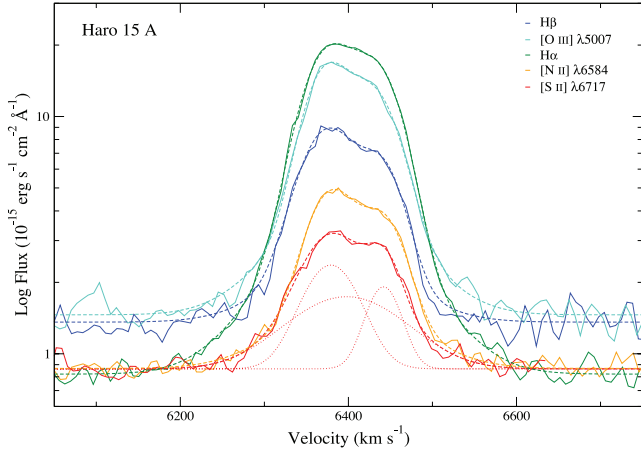


Figure 3. Same set of lines as plotted in Fig. 2 now overlapped in the same diagram. To enhance details at low-luminosity levels, the y-axes are shown in logarithmic scale. The evident similarity among different lines belonging to different elements confirms the presence of a complex kinematical structure. The results of fitting of individual components for the [S II] $\lambda 6717$ forbidden line are included as a reference.

explain by fitting a broad component with a velocity dispersion of about 43 km s^{-1} . Results of the fitting procedure can be seen in Fig. 5; it is worth noting that the logarithmic scale chosen for the y-axis magnifies the 1 per cent residual in the profile wings for H α and [O III] $\lambda 5007$. For the listed lines the derived radial velocities, velocity dispersions and their corresponding errors are listed in

Table 2. The overall H α flux, uncorrected for reddening, is found to be $(9.88 \pm 0.3) \times 10^{-14} \text{ erg s}^{-1} \text{ cm}^{-2}$.

As concluded by López-Sánchez & Esteban (2009), knot B has a much higher ionization degree than the rest of the regions in Haro 15. These authors suggest that this may be a consequence of the extreme youth of this knot. This fact and the low metallicity found in knot B (lower than for the other regions) indicate that it has a different nature, probably being the remnant of a dwarf galaxy which is experiencing a minor interaction with Haro 15 (López-Sánchez 2010).

3.1.3 Haro 15 C

Although the observed spectrum of region C is faint, we were able to identify and fit Gaussian profiles to the H β , [O III] $\lambda 5007$, H α , [N II] $\lambda 6584$ and [S II] $\lambda \lambda 6717, 6731$ lines. Knot C shows one narrow component together with the underlying broad component. However, due to the poor signal of the spectrum, all emission lines were fitted using the H α *NGAUSSFIT* solution as a template, fixing the profile centres and widths, and only allowing the task to fit the profile amplitudes. In Fig. 6 we only show H α since the rest of the intense lines are very noisy due to the low signal-to-noise (S/N) ratio of the spectrum. Table 3 shows the derived kinematical parameters. The overall H α flux, uncorrected for reddening, is $(2.67 \pm 0.07) \times 10^{-15} \text{ erg s}^{-1} \text{ cm}^{-2}$.

3.1.4 Haro 15 E

We detect the presence of a broad profile, suggesting the presence of a double peak together with a flux excess in the strongest emission

Table 2. Results of Gaussian profile fitting to the observed emission lines in Haro 15 A and B. Each emission line is identified by its ion laboratory wavelength and ion name in columns 1 and 2. According to the different fits performed on each line, column 3 identifies each narrow component (1 and 2, where applicable), and a broad component. Radial velocities (V_r) and intrinsic velocity dispersions (σ_{int}) together with their respective errors are expressed in km s^{-1} . The intrinsic velocity dispersions are corrected for the instrumental and thermal widths. Fractional emission measures (EM_f) in per cent.

λ_0	Ion	Comp.	Haro 15 A					Haro 15 B				
			V_r	Error	σ_{int}	Error	EM_f	V_r	Error	σ_{int}	Error	EM_f
4861	H β	Narrow 1	6375.5	0.8	28.8	1.1	55.7	6381.2	0.8	17.3	1.1	23.6
		Narrow 2	6440.1	0.9	20.7	1.1	25.6
		Broad	6390.6	5.2	72.5	2.4	18.7	6393.4	0.8	43.3	1.1	76.4
4959	[O III]	Narrow 1	6373.4	1.1	26.5	1.3	39.0	6383.2	0.8	16.5	1.1	15.5
		Narrow 2	6426.2	1.3	31.9	1.5	38.0
		Broad	6384.4	4.7	64.0	6.0	23.0	6394.4	0.7	40.1	1.1	84.5
5007	[O III]	Narrow 1	6372.7	0.7	24.9	1.1	39.2	6384.1	0.8	15.1	1.1	13.0
		Narrow 2	6429.1	0.8	28.8	1.1	35.4
		Broad	6396.2	1.6	73.0	2.4	25.4	6395.2	0.7	40.2	1.0	87.0
6548	[N II]	Narrow 1	6378.7	1.2	28.6	1.1	53.4	6381.9	1.3	20.6	1.2	50.2
		Narrow 2	6438.3	1.1	21.5	1.3	27.9
		Broad	6405.5	12.1	72.0	14.1	18.7	6395.6	4.2	49.0	4.7	49.8
6563	H α	Narrow 1	6376.1	0.6	27.3	0.8	47.6	6385.0	0.6	20.0	0.8	28.4
		Narrow 2	6436.0	0.6	24.5	0.8	33.0
		Broad	6395.8	2.6	77.8	1.7	19.4	6393.5	0.6	43.7	0.8	71.6
6584	[N II]	Narrow 1	6379.9	0.6	27.5	0.8	46.6	6381.5	0.7	24.3	0.9	59.8
		Narrow 2	6441.9	0.7	24.5	0.9	28.1
		Broad	6399.2	2.1	74.7	2.5	25.3	6392.9	2.3	48.4	2.3	40.2
6717	[S II]	Narrow 1	6379.1	1.2	31.7	0.9	38.1	6382.0	0.8	25.1	0.8	67.1
		Narrow 2	6441.8	1.2	19.1	1.3	16.5
		Broad	6397.9	2.2	65.5	2.4	45.5	6387.8	3.2	52.4	3.3	32.9
6731	[S II]	Narrow 1	6378.3	1.5	32.3	1.7	37.2	6384.9	0.8	23.4	1.0	66.6
		Narrow 2	6442.3	1.1	16.7	1.3	20.2
		Broad	6398.3	3.4	65.3	4.3	42.6	6380.6	4.8	59.0	5.3	33.4

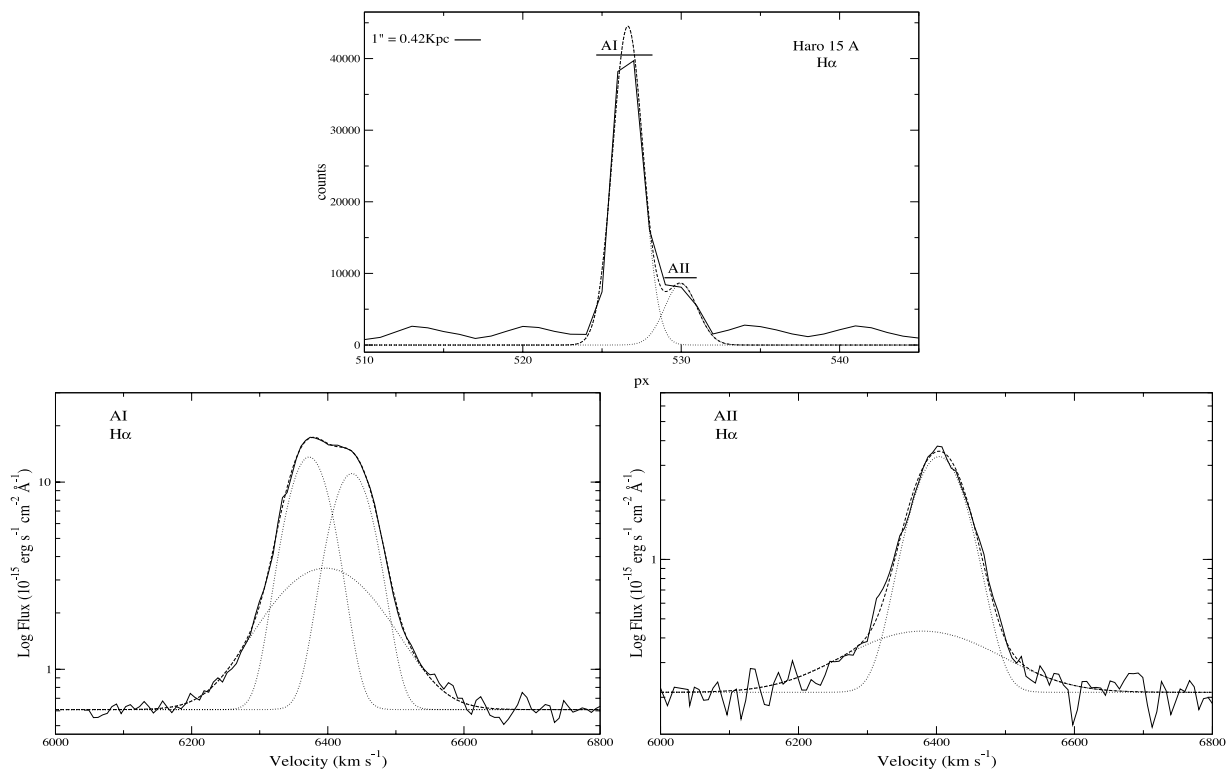


Figure 4. Top panel: intensity distribution along the slit at the peak of the H α emission. Bottom panels: result of profile extraction at the locations of regions A I and A II, together with the result of individual Gaussian profile fitting. To enhance details at low-luminosity levels, the y-axes are shown in logarithmic scale. Two narrow components and a broad one are fitted for A I and only a single narrow and broad component are identified in A II.

lines. We identified and fitted Gaussian profiles to the H β , [O III] λ 5007, H α , [N II] λ 6584 and [S II] λ 6717, 6731 lines. The results of the profile fitting procedure yield two components of similar width. Although both are supersonic profiles, it is not possible to distinguish a broad and narrow component and therefore refer to the identified components as narrow 1 and 2 (see Fig. 6). For the listed lines the derived radial velocities, the velocity dispersions and the corresponding errors are listed in Table 3. The overall H α flux, uncorrected for reddening, is found to be $(4.99 \pm 0.14) \times 10^{-15} \text{ erg s}^{-1} \text{ cm}^{-2}$.

Owing to the poor S/N ratio spectrum we fitted some of the emission lines, such as [N II] λ 6584 and [S II] λ 6717, 6731, using the H α NGAUSSFIT solution, and iterating separately for individual sets of parameters, following the procedure described in Firpo et al. (2010).

3.1.5 Haro 15 F

The observed spectrum of knot F is the weakest one, and hence we only identified and fitted the Gaussian profiles of the H β , [O III] λ 5007 and H α lines. H β and [O III] λ 5007 are in fact very noisy and narrow, rendering impossible the task of fitting multiple Gaussian components (narrow plus broad). The spectral line broadening in their integrated spectra is only observed in the H α line where we could fit a narrow Gaussian component together with the broad one, with velocity dispersions of about 8.3 and 22 km s $^{-1}$, respectively (see Fig. 6). The estimated velocity dispersion for the narrow component in the H α line is subsonic (8 km s $^{-1}$), typical of classic H II regions, although the presence of a broad component is almost exclusive of giant H II regions.

For H α , the derived radial velocity, the velocity dispersions and the corresponding errors are listed in Table 3. The overall H α flux, uncorrected for reddening, is found to be $(1.06 \pm 0.16) \times 10^{-15} \text{ erg s}^{-1} \text{ cm}^{-2}$.

3.2 Radial velocities

The radial velocities for each component of the different knots of Haro 15 are given in the corresponding tables where the results for the profile fits are shown. In Table 4 we list the average radial velocity for each component, together with the corresponding errors. The single component is the result of a single Gaussian fit to the emission-line profiles. In order to compare our results with those of López-Sánchez & Esteban (2009) we have plotted our radial velocities in Fig. 7 relative to the velocity of the galactic centre 6415 km s $^{-1}$ (López-Sánchez 2006), after correcting to the Galactic standard of rest (GSR) using the RVCORRECT task by IRAF. Fig. 7 shows our results together with data presented by López-Sánchez & Esteban (2009) for their long slits with position angles (PA) of 41° and 117°. Regarding the single component velocity, it can be clearly seen that the average radial velocities derived from the emission lines follow nicely those derived by López-Sánchez & Esteban (2009). However, it is worth mentioning that individual velocities of narrow components (n1 and n2) for knot A differ by about 60 km s $^{-1}$. This cannot be easily explained by scatter within galactic rotation, suggesting that their relative velocities are due to mutual orbital motion around their gravity centre.

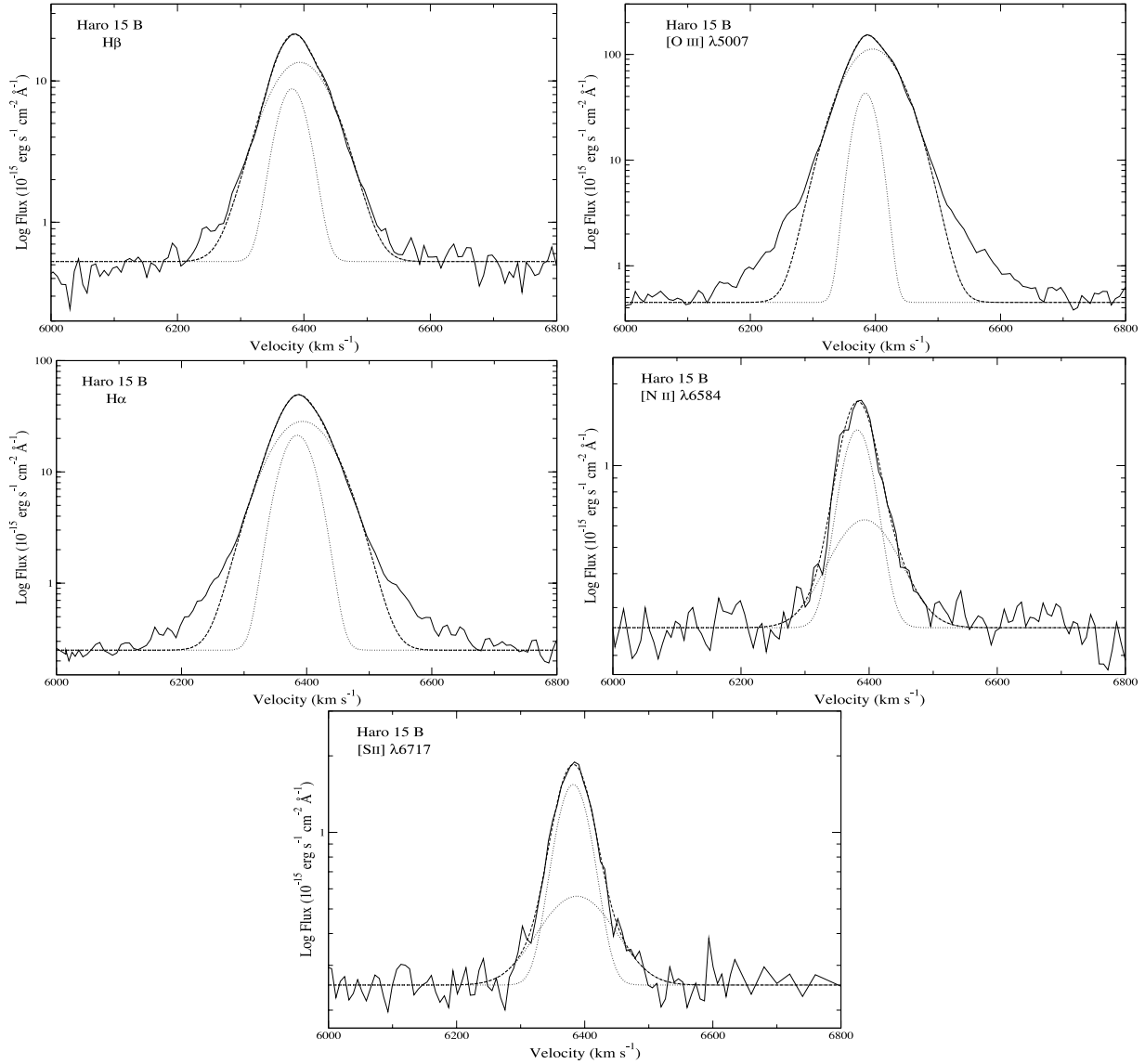


Figure 5. NGAUSSFIT fits with two Gaussian components in the Haro 15 B strongest emission-line profiles, a narrow component and a broad one. In order: H β , [O III] λ 5007, H α , [N II] λ 6584 and [S II] λ 6717. Note that the logarithmic y-scale magnifies the actual low (1 per cent) error in the overall fits.

3.3 Relation between H α luminosities and velocity dispersion

We also explored the influence that the detection of multiple components has on the location of individual giant H II regions in the H α luminosity versus velocity dispersion (σ_{int}) diagram. Table 5 lists the velocity dispersions (for a single Gaussian profile) and H α luminosities derived from our data. These are plotted, together with data from Tables 2 and 3, in Fig. 8. Each knot is labelled from A to F as used throughout this paper. Narrow components are identified with ‘n’, while ‘s’ refers to linewidths measured by fitting a single Gaussian component to the line. Also plotted are data on NGC 6070 and 7479 from Firpo et al. (2010) and giant H II regions from Bosch, Terlevich & Terlevich (2002) together with the regression line fitted by those authors to their ‘young’ giant H II regions. H α luminosities were derived from the fluxes measured directly from the component fitting to our echelle spectra, and using distances as published by de Vaucouleurs et al. (1991) for Haro 15. The correction for reddening could change flux values by a factor up to 1.72 (0.24 in logarithm;

López-Sánchez & Esteban 2009) but, as we cannot determine it for every region, we prefer to list the uncorrected ones.

Similar to what was found by Firpo et al. (2010), the location of the studied regions is far from random. Haro 15 H II regions show a correlation between their luminosities and velocity dispersions. If we focus on the fit of single components they seem to follow the regression found for virialized systems. The outstanding exception to this trend is region A, but this can be attributed to the fact that the profile can be split into two narrow components, resembling the behaviour found for regions NGC 7479-I and 7479-II (Firpo et al. 2010). The narrow components of the composite fits show, as expected, relatively smaller luminosities and velocity widths, but they still lie around the same linear regression. In this case, it is region F that fails to follow the trend but, as mentioned earlier, its low velocity dispersion makes it a very unlikely candidate for a giant H II region. It can be seen from the figure that while narrow components tend to cluster around the $L(\text{H}\alpha) \propto \sigma^4$ relation, single component fits would provide a flatter power-law exponent.

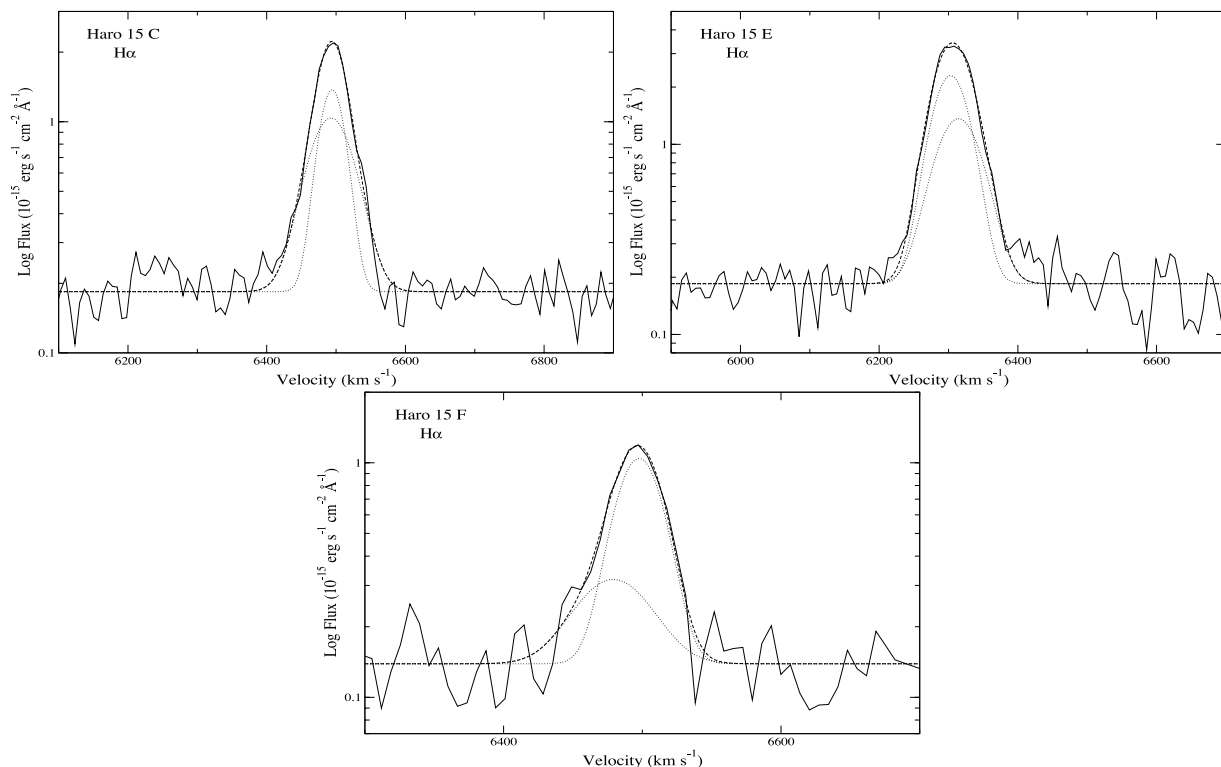


Figure 6. NGAUSSFIT fits with three Gaussian components in the Haro 15 C, E and F H α emission-line profiles, a narrow component and a broad one.

Table 3. Results of Gaussian profile fitting to the observed emission lines in Haro 15 C, E and F. Each emission line is identified by its ion laboratory wavelength and ion name in columns 1 and 2. According to the different fits performed on each line, column 3 identifies the narrow and broad components. Radial velocities (V_r) and intrinsic velocity dispersions (σ_{int}) together with their respective errors are expressed in km s^{-1} . The intrinsic velocity dispersions are corrected for the instrumental and thermal widths. Fractional emission measures (EM_f) in per cent.

λ_0	Ion	Comp.	V_r	Error	σ_{int}	Error	EM_f
<i>Haro 15 C</i>							
6563	$\text{H}\alpha$	Narrow	6494.2	0.4	11.8	0.9	44.5
		Broad	6492.7	0.7	28.5	1.0	55.5
<i>Haro 15 E</i>							
4861	$\text{H}\beta$	Narrow 1	6303.0	0.8	21.4	1.2	48.6
		Narrow 2	6314.4	1.1	28.2	1.4	51.4
5007	[O III]	Narrow 1	6302.9	1.7	23.9	2.2	32.8
		Narrow 2	6307.6	1.2	27.6	1.5	67.2
6563	$\text{H}\alpha$	Narrow 1	6303.0	0.7	21.4	0.9	59.1
		Narrow 2	6314.4	1.0	28.2	1.2	40.9
6584	[N II]	Narrow 1	6306.3	2.0	22.4	2.9	31.2
		Narrow 2	6312.4	2.0	34.2	2.0	68.8
6717	[S II]	Narrow 1	6309.0	1.9	17.6	1.6	24.9
		Narrow 2	6314.3	1.4	27.8	1.5	75.1
6731	[S II]	Narrow 1	6306.1	3.5	14.9	2.3	29.6
		Narrow 2	6314.7	3.4	30.0	2.9	70.4
<i>Haro 15 F</i>							
6563	$\text{H}\alpha$	Narrow	6497.7	1.1	8.3	1.0	75.9
		Broad	6479.1	3.4	22.0	5.7	24.1

This is probably due to the broad component contributing a substantial part of the total H α flux. Although not included in the figure, the broad components are located, as expected, in a parallel sequence shifted towards lower luminosities and/or higher velocity dispersions.

4 SUMMARY

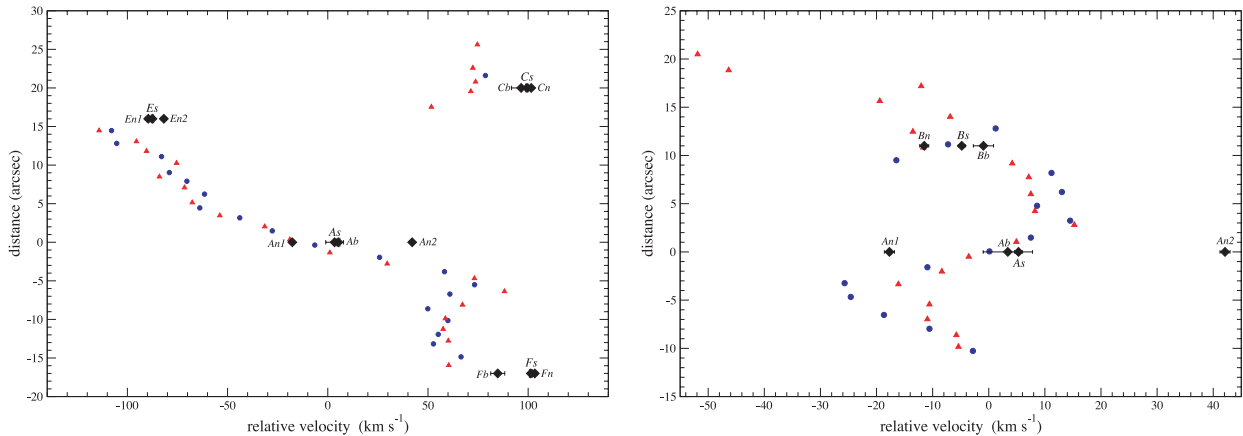
From high-resolution spectroscopy of Haro 15 we have performed a thorough analysis of the emission-line profiles of several knots considering multiple component fits to their profiles. Our results can be summarized as follows.

- (i) Giant H II regions of Haro 15 show a complex structure within the profile of all their emission lines, detected in both recombination and forbidden lines.
- (ii) The brightest emission lines can be split into at least two strong narrow components plus an underlying broad component.
- (iii) Although regions tend to follow the galaxy kinematics, the narrow components of knot A have relative velocities that are too large to be explained by galactic rotation. This behaviour can be explained if we are observing the orbital motion around their gravity centre.
- (iv) Almost all knots follow the relation found between luminosities and velocity dispersions for virialized systems, when considering either single profile fitting or the strong narrow components in more complex fits. Among these, the single one shows a relatively flatter slope.

The presence of more than one component in the Gaussian fits to the emission-line profiles, such as those analysed in this paper, has

Table 4. Average LSR radial velocities for Haro 15 emission-line knots. Column 1 indicates the fitted feature and the remaining columns list the average radial velocity for each knot and its uncertainty, both in km s^{-1} .

Comp.	$\langle V_r \rangle$	Error	$\langle V_r \rangle$	Error	$\langle V_r \rangle$	Error	$\langle V_r \rangle$	Error	$\langle V_r \rangle$	Error
	<i>Haro 15 A</i>		<i>Haro 15 B</i>		<i>Haro 15 C</i>		<i>Haro 15 E</i>		<i>Haro 15 F</i>	
Single	6420.3	0.7	6410.2	0.6	6514.4	0.6	6327.5	0.6	6516.3	0.7
Narrow 1	6397.3	0.9	6403.5	0.8	6516.5	1.3	6325.4	1.4	6518.3	1.2
Narrow 2	6457.1	0.9	6333.2	1.3
Broad	6418.4	4.4	6414.1	1.8	6511.5	4.8	6499.8	3.5

**Figure 7.** Position versus velocity diagrams for the observed knots in Haro 15. $\text{H}\alpha$ radial velocity results, relative to knot A, are superimposed on the data by López-Sánchez & Esteban (2009) for slit positions PA 41° (left-hand panel) and PA 117° (right-hand panel). The $\text{H}\alpha$ and $[\text{O III}] \lambda 5007$ data of López-Sánchez & Esteban (2009) in Haro 15 are identified by blue circles and red triangles, respectively.**Table 5.** Intrinsic velocity dispersions (σ_{int}) and the $\text{H}\alpha$ luminosity ($L(\text{H}\alpha)_s$) for a fitted single Gaussian component, together with their associated errors, expressed in km s^{-1} and erg s^{-1} , respectively. We add the $\text{H}\alpha$ luminosity ($L(\text{H}\alpha)_{\text{overall}}$) obtained from the overall $\text{H}\alpha$ flux, uncorrected for reddening, and its error, in erg s^{-1} .

Knot	σ_{int}	$L(\text{H}\alpha)_s$	$L(\text{H}\alpha)_{\text{overall}}$
Haro 15 A	47.3 ± 0.9	$4.9 \pm 0.7 \times 10^{40}$	$4.9 \pm 0.7 \times 10^{40}$
Haro 15 B	34.4 ± 0.8	$8.6 \pm 1.2 \times 10^{40}$	$8.9 \pm 1.3 \times 10^{40}$
Haro 15 C	19.3 ± 0.8	$2.3 \pm 0.3 \times 10^{39}$	$2.4 \pm 0.3 \times 10^{39}$
Haro 15 E	24.4 ± 0.9	$4.5 \pm 0.6 \times 10^{39}$	$4.5 \pm 0.6 \times 10^{39}$
Haro 15 F	11.6 ± 0.8	$9.1 \pm 1.3 \times 10^{38}$	$9.5 \pm 1.3 \times 10^{38}$

been discussed in several previous studies. Hägele et al. (2007, 2009, 2010) showed fits that involved the existence of broad and narrow components for the emission lines of the ionized gas in circumnuclear star-forming regions. Furthermore, Firpo et al. (2010) were able to detect two distinct components within the narrow feature of the emission lines in the brightest giant H II regions NGC 7479-I and 7479-II. Although we still lack the number of objects needed to support a generalization of this trend, these data show that the presence of multiple kinematical components among extragalactic star-forming regions cannot be overlooked. They might have a strong impact on subsequent analyses that rely on basic parameters,

such as the velocity dispersion and chemical abundance of the ionized gas, the inferences about the nature and strength of the source of ionization or the classification of the activity in the central regions of galaxies.

It is necessary to map these regions with high spectral and spatial resolution and much better S/N ratio to disentangle the origin of these different components. 2D spectroscopy performed with the Integral Field Unit is the ideal tool to tackle this issue.

ACKNOWLEDGMENTS

We are grateful to the director and staff of LCO for technical assistance and warm hospitality. We appreciate the comments and suggestions by the referee, Ángel R. López-Sánchez, which significantly improved this paper. This research has made use of the NASA/IPAC Extragalactic Database (NED) which is operated by the Jet Propulsion Laboratory, California Institute of Technology, under contract with the National Aeronautics and Space Administration. Support from the Spanish Ministerio de Educación y Ciencia (AYA2007-67965-C03-03, AYA2010-21887-C04-03) and partial support from the Comunidad de Madrid under grant S2009/ESP-1496 (ASTROMADRID) are acknowledged. VF and GB would like to acknowledge the hospitality of the Astrophysics Group of the UAM during the completion of this work.

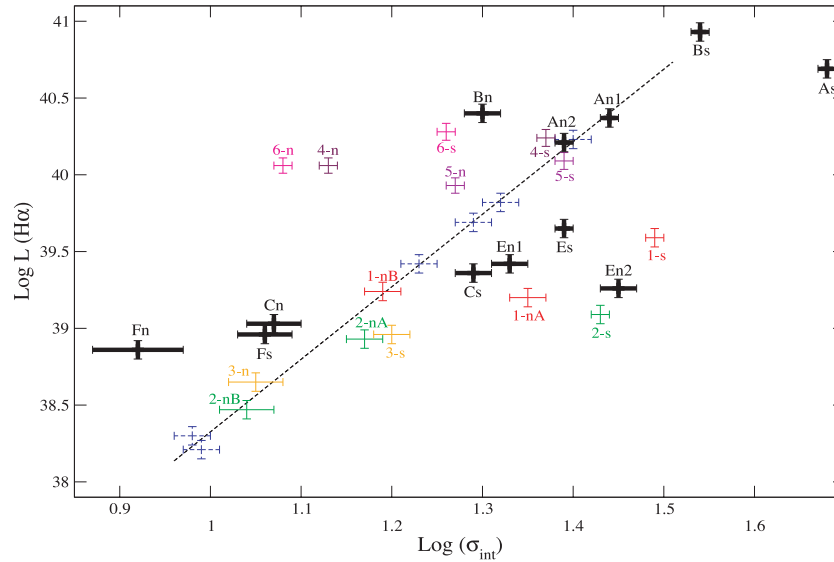


Figure 8. $\log(L)$ – $\log(\sigma)$ relation for our H II regions. Luminosities and velocity dispersions are derived from our spectrophotometric data. The plot includes results from narrow components (labelled as ‘n’) and single profile fits (labelled as ‘s’). We add the data from Firpo et al. (2010) (‘n’, ‘nA’ and ‘nB’ for narrow, and ‘g’ for single components) identified by coloured solid error bars and with numbers (from 1 to 6): NGC 7479-I (1) in red, NGC 7479-II (2) in green, NGC 7479-III (3) in yellow, NGC 6070-I (4) in maroon, NGC 6070-II (5) in violet and NGC 6070-IV (6) in magenta. A few giant H II regions from Bosch et al. (2002) (blue dashed error bars) together with their linear fit to their ‘young’ giant H II regions are plotted as a reference value. The luminosities are not corrected for extinction.

REFERENCES

- Bohlin R. C., Dickinson M. E., Calzetti D., 2001, *AJ*, 122, 2118
 Bosch G., Terlevich E., Terlevich R., 2002, *MNRAS*, 329, 481
 Cairós L. M., Vílchez J. M., González Pérez J. N., Iglesias-Páramo J., Caon N., 2001a, *ApJS*, 133, 321
 Cairós L. M., Caon N., Vílchez J. M., González-Pérez J. N., Muñoz-Tuñón C., 2001b, *ApJS*, 136, 393
 Chu Y. H., Kennicutt R. C. J., 1994, *ApJ*, 425, 720
 Cumming R. J., Fathi K., Östlin G., Marquart T., Márquez I., Masegosa J., Bergvall N., Amram P., 2008, *A&A*, 479, 725
 de Vaucouleurs G., de Vaucouleurs A., Corwin H. G., Buta R. J., Paturel G., Fouque P., 1991, *Third Reference Catalogue of Bright Galaxies*, Version 3.9. Springer-Verlag, Berlin
 Firpo V., Bosch G., Morrell N., 2005, *MNRAS*, 356, 1357
 Firpo V., Bosch G., Hägele G. F., Morrell N., 2010, *MNRAS*, 406, 1094
 García-Rojas J., Esteban C., Peimbert A., Peimbert M., Rodríguez M., Ruiz M. T., 2005, *MNRAS*, 362, 301
 Hägele G. F., Díaz Á. I., Cardaci M. V., Terlevich E., Terlevich R., 2007, *MNRAS*, 378, 163
 Hägele G. F., Díaz Á. I., Cardaci M. V., Terlevich E., Terlevich R., 2009, *MNRAS*, 396, 2295
 Hägele G. F., Díaz Á. I., Cardaci M. V., Terlevich E., Terlevich R., 2010, *MNRAS*, 402, 1005
 Hammer F., Gruel N., Thuan T. X., Flores H., Infante L., 2001, *ApJ*, 550, 570
 Hippelein H. H., 1986, *A&A*, 160, 374
 Hoyos C., Guzmán R., Bershadsky M. A., Koo D. C., Díaz A. I., 2004, *AJ*, 128, 1541
 Hoyos C., Guzmán R., Díaz A. I., Koo D. C., Bershadsky M. A., 2007, *AJ*, 134, 2455
 Hunter D. A., Gallagher I. J. S., 1985, *AJ*, 90, 1457
 Kong X., Cheng F. Z., Weiss A., Charlot S., 2002, *A&A*, 396, 503
 Kovo O., Contini T., 1999, in van der Hucht K. A., Koenigsberger G., Ekenens P. R. J., eds, *Proc. IAU Symp. 193, Wolf-Rayet Phenomena in Massive Stars and Starburst Galaxies*. Astron. Soc. Pac., San Francisco, p. 604
 López-Sánchez Á. R., 2006, PhD thesis, Instituto de Astrofísica de Canarias
 López-Sánchez Á. R., 2010, *A&A*, 521, 63
 López-Sánchez Á. R., Esteban C., 2008, *A&A*, 491, 131
 López-Sánchez Á. R., Esteban C., 2009, *A&A*, 508, 615
 López-Sánchez Á. R., Esteban C., 2010, *A&A*, 516, 104
 López-Sánchez Á. R., Esteban C., Rodríguez M., 2004, *A&A*, 428, 425
 López-Sánchez Á. R., Esteban C., García-Rojas J., 2006, *A&A*, 449, 997
 Mazzarella J. M., Bothun G. D., Boroson T. A., 1991, *AJ*, 101, 2034
 Melnick J., Tenorio-Tagle G., Terlevich R., 1999, *MNRAS*, 302, 677
 Muñoz-Tuñón C., Tenorio-Tagle G., Castañeda H. O., Terlevich R., 1996, *AJ*, 112, 1636
 Osterbrock D. E., Fulbright J. P., Martel A. R., Keane M. J., Trager S. C., Basri G., 1996, *PASP*, 108, 277
 Östlin G., 1998, PhD thesis, Uppsala University
 Relaño M., Beckman J. E., 2005, *A&A*, 430, 911
 Roy J. R., Arsenault R., Joncas G., 1986, *ApJ*, 300, 624
 Rozas M., Richer M. G., López J. A., Relaño M., Beckman J. E., 2006, *A&A*, 455, 539
 Schaerer D., Contini T., Pindao M., 1999, *A&AS*, 136, 35
 Shi F., Kong X., Li C., Cheng F. Z., 2005, *A&A*, 437, 849
 Terlevich R., Melnick J., 1981, *MNRAS*, 195, 839

This paper has been typeset from a \LaTeX file prepared by the author.